CrystEngComm

PAPER

Synthesis, optical and photovoltaic properties of bismuth sulfide nanorods

Hsueh-Chung Liao,[a] Ming-Chung Wu,[ab] Meng-Huan Jao,[a] Chih-Min Chuang,[c] Yang-Fang Chen[d] and Wei-Fang Su*[a]

Bismuth sulfide (Bi_2S_3) nanorods exhibit a low band gap, a high absorbance coefficient and good dispersity. In this study, the synthesis conditions of Bi_2S_3 nanorods were systematically investigated to obtain nanorods of a desired dimension, with high aspect ratios and good crystallinity. The as synthesized Bi_2S_3 nanorods, 37.2 nm in length and 6.1 nm in width, have a low band gap of ∼1.4 eV with a conduction band and valence band of −3.8 eV and −5.2 eV, respectively. The nanorods were blended with poly(3-hexylthiophene) (P3HT) at a weight ratio of 1 : 1 to form a light harvesting P3HT : Bi_2S_3 hybrid film. The incorporated Bi_2S_3 nanorods can not only contribute light harvesting but also lead to a more ordered structure of the P3HT phase and a more efficient π–π* transition. Surface potential mapping of the hybrid film, measured by Kelvin probe force microscope (KPFM), shows a significantly negative shift (−34 mV) under white light illumination, which indicates carrier dissociation and the accumulation of negative charge on top of the hybrid film. The photovoltaic characteristics of the devices were also observed for those based on the P3HT : Bi_2S_3 hybrid film. This novel P3HT : Bi_2S_3 hybrid material provides a new candidate for the fabrication of low-cost and environmentally friendly polymer/inorganic hybrid solar cells.

1. Introduction

Over the last decade, semiconducting nanocrystal have shown great potential in the application of various optoelectrical technologies, such as photon source,[1–4] biological imaging,[5–7] light-emitting diodes[8–10] and solar energy conversion,[11–15] etc. The chemical synthesis enables exquisite control over the composition, dimension and shape of the nanocrystals, leading to unique and shape-related functionalities. An important way used to manipulate the shape is the passivation of the nanocrystal surface by a surface ligand, which has afforded materials in the shape of dots, rods and tetrapods.[16–18] The rod and wire shapes have particular potential in electronic applications as they provide high aspect ratios and, thus, a direct pathway for electrical transport.

For solar energy technology applications, polymer-based photovoltaic devices have attracted considerable interest owing to their advantages, which include low-cost, a low weight, a solution fabrication process, a large area and flexibility.[19–21] The conducting polymer, however, typically exhibits lower conductivity compared with inorganic semiconductors. The combination of conducting polymers and inorganic semiconducting nanocrystals was hence developed as hybrid materials for solar cell applications and they are known as hybrid solar cells.[22–32] The intimate mix of the conducting polymer and the inorganic semiconducting nanocrystal, which is usually in a rod or tetrapod shape, is the most promising material for such devices due to the formation of a bulk heterojunction. The percolated network constructed by the nanorod or tetrapod provides a direct pathway for carrier transport and reduces the opportunity of inefficient electron transport, such as hopping between the nanocrystals. Several semiconducting nanocrystals have been used in hybrids with conducting polymers, such as CdSe,[26,27,32] CdS,[28,29] TiO_2[22,25] and ZnO[24,30,31] etc. Significant efficiencies of over 2–3% have been obtained.[25,32] Furthermore, over the last few years, scientists have started to synthesize nanocrystals with a low band gap (<1.8 eV) as a promising approach to harvest more sun light. Hence, low band gap materials, such as PbS,[33] PbSe[34] and $CuInSe_2$[35] are candidates for hybrid solar cell applications. Sargent et al. demonstrated the existence of a photovoltaic effect in devices made from MEH-PPV (poly [2-methoxy-5-(2′-ethylhexyloxy-p-phenylene vinylene)])/PbS nanocrystal hybrids.[33] Their research successfully extended the photovoltaic response to wavelengths of 1400–1600 nm using low band gap nanocrystals of PbS (band gap of bulk material = 0.37 eV). Additionally, Arici et al. demonstrated the bulk heterojunction made between P3HT/$CuInSe_2$ hybrids exhibiting a power conversion efficiency of 0.15% under AM 1.5

[a]Department of Materials Science and Engineering, National Taiwan University, No. 1, Sec. 4, Roosevelt Road, Taipei 10617, Taiwan. E-mail: suwf@ntu.edu.tw; Fax: +886 2 33664078; Tel: +886 2 33664078
[b]Department of Chemical and Materials Engineering, Chang Gung University, No.259, Wenhua 1st Road, Guishan Township, Taoyuan County 333-02, Taiwan
[c]Institute of Nuclear Energy Research, Longtan Township, No. 1000, Wenhua Road, Taoyuan County 32546, Taiwan
[d]Department of Physics, National Taiwan University, No. 1, Sec. 4, Roosevelt Road, Taipei 10617, Taiwan

illumination.[35] However, due to concern over the use of toxic elements, including Se, Pb and Cd, the usage of such elements remains a limitation due to environmental issues and this has led to the development of other low band gap nanocrystals. Chen *et al.* demonstrated photovoltaic devices based on P3HT and iron disulfide (Fe_2S) hybrids exhibiting a power conversion efficiency of 0.16%.[36] Bi_2S_3 nanocrystals are a promising semiconductor, which has been applied in photodetectors;[37] however, no photovoltaic properties have been reported to date. Therefore, in the present study, Bi_2S_3 nanorods with an absorption coefficient[38] of around 10^4 cm^{-1} and direct band gap of 1.4 eV were investigated. The synthesis conditions were first systematically investigated in order to tune the dimensions, aspect ratio and crystallinity. The nanorods were blended with P3HT to form a bulk heterojunction hybrid film of which the optical, electrical and optoelectrical properties were characterized. Finally, a photovoltaic device based on the P3HT : Bi_2S_3 nanorods hybrid was fabricated. The advantages of cheapness, abundance and non-toxic elements make the Bi_2S_3 nanorod a promising material in hybrid solar cell applications.

2. Experimental

2.1 Synthesis of Bi_2S_3 nanorods

All chemicals were used as received without further purification. The Bi_2S_3 nanorods were prepared by a solution process according to the literature.[39] Typically, 1 g of bismuth chloride ($BiCl_3$, Arcros 99.999%) and 4.2 ml of oleylamine (Acros, 80–90%) were mixed in a 50 ml three-necked round-bottomed flask equipped with a reflux condenser and then reacted at 170 °C for 20 min under an Ar flow. Afterward, 10.4 ml oleylamine solution of 0.5 g sulfur (S, Acros 99.999%) was injected into the flask and the solution turned red–brown immediately. In order to get nanorods with the desired aspect ratio and size distribution, the reaction conditions, including reaction temperature and reaction time, were varied (110 °C, 130 °C and 150 °C for 30 min, and 110 °C for 5 min, 30 min, 120 min and 240 min). After the growth and crystallization of the nanorods, the reaction was quenched by injecting cold hexane followed by centrifugation at 10 000 rpm for 10 min. The precipitate was ultrasonically dissolved in toluene and heated at 80 °C in an oven overnight. The soluble and insoluble parts were separated by centrifugation at 6000 rpm for 3 min. After discarding the insoluble nanorods, the upper Bi_2S_3 nanorods in the supernatant were precipitated out by the addition of ethanol followed by centrifugation at 10 000 rpm for 10 min. The final solid product dispersed very well in organic solvents, such as toluene, chlorobenzene and chloroform. The yield of the Bi_2S_3 nanorods in the present work is nearly 7–8%. In order to obtain refined nanorods with a uniform size and good crystallinity, a low reaction temperature of 80 °C was employed and the reaction left overnight. A lot of large nanocrystals were discarded after this step, which leads to a relatively low yield. Additionally, the Bi_2S_3 nanorods synthesized under different conditions exhibited similar yields.

2.2 Fabrication of the P3HT : Bi_2S_3 photovoltaic device

P3HT with a molecular weight of 70.0 kDa and PDI with a molecular weight of 1.45 and regio-regularity greater than 99% were synthesized according to the litrature.[40] The transparent indium tin oxide (ITO) electrode (Merck) with a sheet resistance of 15 Ω was ultrasonically cleaned with a series of solvents (ammonia/H_2O_2/deionized water, methanol and isopropanol) followed by oxygen plasma treatment. A hole transport layer, poly(3,4-ethylenedioxythiophene)–poly(styrenesulfonate) (PEDOT) : PSS), of 40 nm was then spin coated on the substrate. After heating at 120 °C for 30 min, the active layer of the P3HT : Bi_2S_3 film made from the hybrid of P3HT and Bi_2S_3 at a 1 : 1 wt/wt ratio in a chlorobenzene/toluene co-solvent was deposited by spin coating on the top of the PEDOT : PSS layer. An upper Al cathode (~100 nm) was thermal evaporated at ~2×10^{-6} torr to form devices with an area of 0.05 cm^2. Sandwiched between the active layer and the cathode was a 20 nm electron collecting layer deposited by spin coating a TiO_2 nanorod solution (pyridine, 5 mg ml^{-1}). The high aspect ratio TiO_2 nanorods were prepared according to the literature.[22]

2.3 Characterization of Bi_2S_3 nanorods and P3HT : Bi_2S_3 hybrids

The film thickness of both pristine P3HT and P3HT : Bi_2S_3 films were characterized by α-stepper (Veeco, Dektak 6M 24383). The transmission electron microscope (TEM) and high resolution transmission electron microscope (HRTEM) images of the Bi_2S_3 nanorods were obtained by a JEOL JEM-1230 microscope operating at 100 keV and a FEI Tecnai G2 T20 microscope operating at 200 keV, respectively. By determining the dimensions of the nanorods appearing in the TEM images, information on the dimensions of Bi_2S_3 under different synthesis conditions was obtained. The crystalline structure was studied using X-ray diffraction (PANalytical X' Pert PRO with filtered Cu Kα radiation (λ = 1.54Å)). A glass boat was fabricated as a powder sample holder for the X-ray diffraction study. In order to compare the diffraction peaks among the different synthesis conditions, the amount of each powder sample was controlled (to ensure it was identical) by filling the boat and carefully removing the excess. Cyclic voltammetry (CV) was performed (CHI 600B) to analyze the conduction band (CB) and valence band (VB) of the Bi_2S_3 nanorods. The nanorods were dissolved in a 0.05 M solution of tetra-*n*-butyl-ammonium hexafluorophosphate (Bu_4NPF_6, Aldrich, 98%) in tetrahydrofuran (J. T. Baker, 99.99%). A concentration of 0.1 M tetra-*n*-butylammonium hexafluorophosphate was used as the supporting electrolyte. The glass carbon electrode, the Ag/$AgNO_3$ electrode and the platinum wire were used as the working, reference and counter electrodes, respectively. A ferrocene/ferrocinium (Fc/Fct) couple (Acros, 98%) was used as the internal reference and all potentials were calibrated with Fc/Fct. For the optical measurement, we utilized UV–visible spectroscopy (Perkin–Elmer Lambda 35) and spectro-fluorometry (Perkin–Elmer LS-55) to measure the ultraviolet–visible absorption spectra and steady-state photoluminescence spectra, respectively. The surface potential of the P3HT : Bi_2S_3 hybrid film was analyzed by KPFM (Digital Instruments, Nanoscopes III) at room temperature using a conductive tip with a resonance frequency of 75 kHz, on average, and coated with a platinum–iridium alloy. To prepare the samples for KPFM measurements, typically we first spin coated PEDOT : PSS on to a conducting substrate (ITO). After
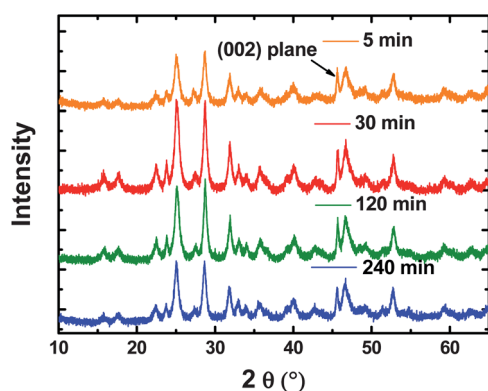
heating at 120 °C for 30 min, P3HT : Bi_2S_3 thin films were deposited by spin coating on top of the PEDOT : PSS layer followed by grounding of the PEDOT : PSS layer to a metal substrate *via* a silver paste. It is noteworthy that the P3HT : Bi_2S_3 layer must not connect with the silver paste to ensure a single path through the hybrid layer/PEDOT : PSS/silver paste/metal substrate for hole transport. The J–V curves of the photovoltaic devices based on P3HT : Bi_2S_3 were characterized under AM 1.5 radiation (100 mW cm^{-2}).

3. Results and discussion

We investigated the appropriate synthesis conditions of Bi_2S_3 nanorods for applications in hybrid solar cells. Fig. 1 shows the X-ray diffraction patterns of the Bi_2S_3 nanorods grown at 130 °C for different reaction times of 5, 30, 120 and 240 min. The XRD patterns of the nanorods are identical to that of the Bi_2S_3 nanowires or nanorods reported in the literature.[41] Bi_2S_3 nanorods present peaks assignable to the orthorhombic structure (cell constants $a = 11.15$ Å, $b = 11.30$ Å and $c = 3.98$ Å; JCPDS No. 43-1471). No obvious peak attributable to bismuth or sulfur could be observed. According to the literature,[41] Bi_2S_3 nanorods elongate along the [002] direction. Hence, the arrow pointing to the (002) diffraction peak in Fig. 1, around 45.1°, represents the crystal plane of the longitudinal direction. We compared the (002) diffraction peak of samples synthesized at various reaction times. Obvious differences in the peak intensity and peak area among the four samples were observed. The calculated data, including the peak intensity, peak area, full width at half maximum (FWHM) and grain size of the Bi_2S_3 nanorods are listed in Table 1. The grain sizes of the Bi_2S_3 nanorods were estimated by the Scherrer equation:

$$D_{hkl} = \frac{0.9\lambda}{\beta_{hkl}\cos\theta}$$

where D_{hkl} is the crystalline grain size along the [hkl] direction and 0.9 is the shape factor, K. λ is the X-ray wavelength, which is 1.54 Å in our measurement. β_{hkl} is the full width at half maximum of an (hkl) diffraction (in radians), and θ is the Bragg angle. From Table 1 we can see that the grain sizes don't show a significant difference (range: 24.0–25.4 nm) among the four samples. However, when comparing the peak intensities and peak areas,

the nanorods with a reaction time of 30 min present the most intense peak and the largest peak areas. When extending the reaction time to 120 and 240 min, respectively, both the peak intensities and peak areas are diminished. Since the peak intensity and area are strongly dependent on the crystallinity, we conclude that the nanorods grown for 30 min yield the best crystallinity based on the identical amounts of investigated powders. The active layer of our hybrid solar cell is typically 120–150 nm in thickness. Hence, controlling the length and the aspect ratio of the nanorods is critical for obtaining well blended and smooth hybrid films. Hence, the dimension variation with different reaction times was examined. Fig. 2 (a, c, e, g) show the TEM images of Bi_2S_3 nanorods synthesized at 130 °C for different reaction times and Fig. 2 (b, d, f, h) are the length distributions of the Bi_2S_3 nanorods. The results are summarized in Table 1. We observe that the mean rod length reached 33.6 nm within 5 min but with a relatively large size distribution from 10 nm to 50 nm. When the reaction time was extended to 30 min, the maximum length of the nanorods remained the same. Only a slight increase in the average length is observed (from 33.6 nm to 37.2 nm) due to the elongation of the shorter rods (10–20 nm). These changes lead to a narrower size distribution (standard deviation reduced from 9.2 nm to 6.2 nm). However, we were surprised by the size change when we increased the growth time to a few hours, as shown in Fig. 2 (e, f, g, h). Instead of an increase in the length, the average rod length significantly dropped to 25.5 and 24.5 nm for reaction times of 120 and 240 min, respectively. Furthermore, nanorods with a length over 40 nm were not observed, while those with a length of 5–20 nm appeared again. Therefore, we deduced that after the hot injection of sulfur, the growth of the nanorods must be rapid upon interaction of the sulfur with Bi in solution and completes within tens of minutes. The reaction from 5 min to 30 min under vigorous stirring can ensure the homogeneous growth of all nanorods and narrow the size distribution. However, when the reaction time is extended to a few hours, two reasons may be suspected as being responsible for the reduced rod length: (1) the continued formation of the nucleus, and (2) Bi_2S_3 nanorods "break" at the tips, yielding shorter nanorod pieces or even nanodots, as shown in Fig. 2(g). Some literature reports have detailed this observation and simulated the breaking of nanowires or nanorods induced from crystal defects or crystal mismatches.[42,43] However, to date, no reference has demonstrated the breaking of Bi_2S_3 nanowires or nanorods during their formation.

Additionally, for the width variation of the rods, the diameter gradually increases as the reaction time increases (Table 2). As a result, nanorods with lower aspect ratios, or even nanodots, were obtained when the reaction time was extended to 240 min (Fig. 2(g)). Considering the application of the polymer : nanocrystal hybrid, the opportunity for inter-nanocrystal hopping during carrier transport may be increased by use of the lower aspect ratio nanorods or nanodots if it is assumed that the nanocrystals are inter-connected to each other and construct a percolated network in the polymer matrix. Therefore, in order to reduce the insufficient transport pathway of inter-nanocrystal hopping, a reaction time of 30 min may be regarded as the most appropriate reaction time for nanorods that will be used as electron acceptors in hybrid solar cells. The nanorods have the

Fig. 1 XRD patterns of Bi_2S_3 nanorods grown at 130 °C for different reaction times.

Table 1 Analysis of crystalline quality of Bi_2S_3 nanorods synthesized at 130 °C for different reaction time

Reaction time (min)	Peak intensity (a.u.)	Peak area (a.u.)	FWHM (nm)	Crystalline grain size (nm)
5	275	105	0.36	24.0
30	380	135	0.34	25.4
120	328	110	0.34	25.4
240	272	101	0.35	24.7
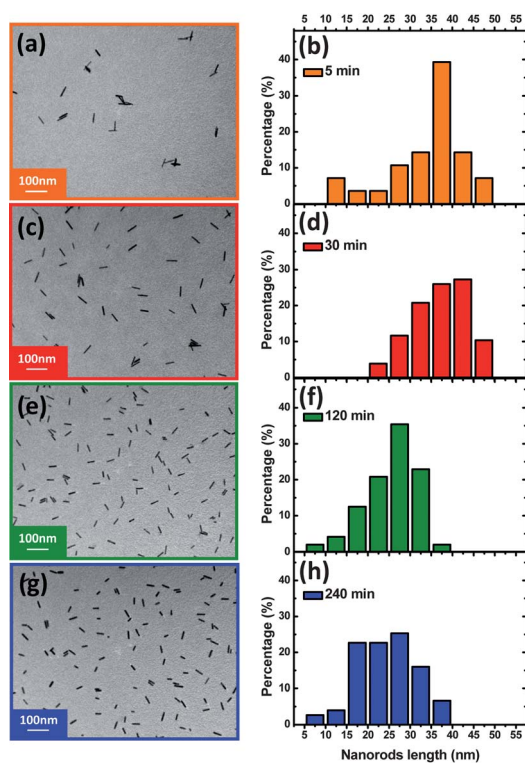
Fig. 2 TEM images (a, c, e, g) and length distributions (b, d, f, h) of Bi_2S_3 nanorods reacted at 130 °C for (a, b) 5 min, (c, d) 30 min, (e, f) 120 min and (g, h) 240 min.

desired aspect ratio for ease of dispersion in P3HT and high crystallinity, which is beneficial for fast electron transport. The HRTEM image of Bi_2S_3 nanorods reveals their high crystallinity when they were reacted at 130 °C for 30 min (Fig. 3).

Another synthesis parameter we adjusted was the reaction temperature of the nanorods, including temperatures of 110 °C, 130 °C and 150 °C at a fixed reaction time of 30 min. The TEM images and size distributions of the nanorods are shown in Fig. 4. The calculated dimensions of the nanorods are summarized in Table 2. We find that the nanorods grown at 110 °C exhibit aggregation and a large size distribution from 10 to 65 nm (standard deviation = 16.5 nm, 42% of the length of the nanorod). In contrast, the nanorods grown at higher temperatures (130 °C and 150 °C) disperse well and are more uniform with regards to their size distributions (standard deviation ~6.2, 17% of the nanorod length and 5.1 nm, 18% of the nanorod length at 130 °C and 150 °C, respectively). Additionally, increasing the reaction temperature to 150 °C leads to a reduction of the length and an increase of the width. For the same concern mentioned above regarding a more efficient carrier transport pathway, larger aspect ratios are preferred. Consequently, we consider 130 °C to be the most suitable reaction temperature to meet our needs. The Bi_2S_3 nanorods that were 37.2 nm in length and 6.1 nm in diameter were adopted in further investigations of the Bi_2S_3 : P3HT hybrid.

The energy levels of semiconducting nanocrystals are crucial when it acts as an electron acceptor or hole donor. A type II alignment between the polymer/nanocrystals ensures charge separation at the interface. What's more, the open circuit voltage of the photovoltaic devices is theoretically equal to the energy gap between the highest occupied molecular orbital (HOMO) of the polymers and the CB of the nanocrystals. Fig. 5(a) plots the current obtained under both a positive and negative bias. By resolving the threshold point for the oxidation and reduction peaks, the calculated CB and VB are −3.8 eV and −5.2 eV, respectively, yielding a band gap of 1.4 eV. Fig. 5(b) depicts the energy band diagram of the Bi_2S_3 nanorods aligned with the layers in typical polymer solar cell structures. The P3HT and Bi_2S_3 nanorods construct a type II contact with an energy gap of 1.2 eV between the HOMO of the polymer and the CB of the nanocrystals. The optical properties of Bi_2S_3 nanorods have also been investigated. Fig. 5(c) shows the absorption spectrum of Bi_2S_3 and the inset shows a plot of $(\alpha h\nu)^{2/3}$ verses $h\nu$, where α is the absorption coefficient (which can be obtained by the

Table 2 Dimension analysis of Bi_2S_3 synthesized under different reaction conditions

Reaction temperature (min)	Reaction time (min)	Average rod length (nm)	Average rod width (nm)	Aspect ratio
130	5	33.6 ± 9.2	5.1 ± 1.4	6.6
130	30	37.2 ± 6.2	6.1 ± 0.9	6.1
130	120	25.5 ± 6.1	6.8 ± 1.1	3.8
130	240	24.5 ± 6.9	8.5 ± 1.2	2.9
110	30	39.1 ± 16.5	5.3 ± 1.0	7.3
130	30	37.2 ± 6.2	6.1 ± 0.9	6.1
150	30	28.8 ± 5.1	7.4 ± 1.1	3.9

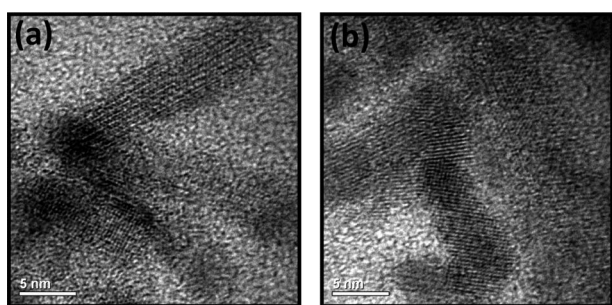**Fig. 3** (a, b) HRTEM images of Bi_2S_3 nanorods reacted at 130 °C for 30 min.

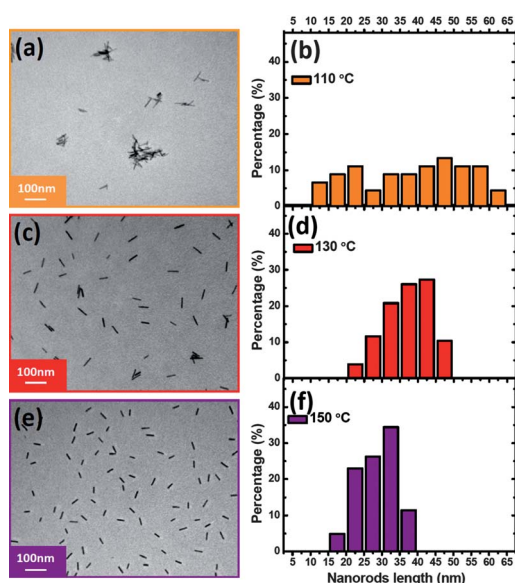**Fig. 4** TEM images (a, c, e) and length distributions (b, d, f) of Bi_2S_3 nanorods reacted for 30 min at 110 °C (a, b), 130 °C (c, d) and 150 °C (g, h).

Fig. 5 (a) A CV curve of the Bi_2S_3 nanorods, (b) the energy band diagram of Bi_2S_3 together with the layers in a typical polymer solar cell and (c) the absorption spectrum of the Bi_2S_3 nanorods.

absorbance, A, following Beer's law, $A = \alpha l$, l is the optical path length), h is Planck's constant and ν is the frequency of the optical radiation. Following the relation of $\alpha h\nu = (h\nu - Eg)^{3/2}$, the plot in the inset has an intercept of nearly 1.55 eV, indicating the optical bandgap (Eg) of 1.55 eV, which is consistent with the onset of the absorption spectrum (~750 nm, Fig. 5(c)) and slightly larger than the value obtained from the cyclic voltammetry measurements (1.4 eV). The relatively strong absorbance in the visible region shows its potential to increase sun light harvesting in hybrid materials.

The UV–vis absorption spectrum of $P3HT : Bi_2S_3$ is shown in Fig. 6(a). Pristine P3HT, for comparison, was prepared under an identical fabrication process including the solvents, concentrations and parameters of the spin coating. We can observe that the absorption spectra of $P3HT/Bi_2S_3$ exhibits a similar shape to pristine P3HT, indicating that the absorption behaviour is still dominated by the polymer P3HT. This strong domination may be attributed to the large absorption coefficient of P3HT of 1.7×10^5 cm^{-1}, which is an order of magnitude larger than that of Bi_2S_3 (~10^4 cm^{-1}). The absorbance difference between pristine P3HT and the $P3HT : Bi_2S_3$ hybrid obtained by subtracting the two

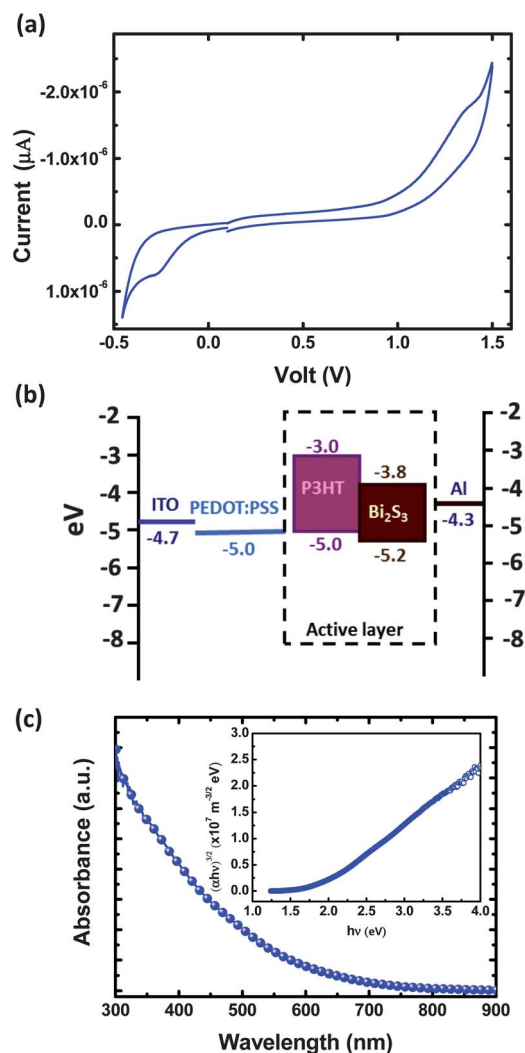spectra is shown in Fig. 6(b). The optical absorption of Bi_2S_3 ranged from 380 nm to 800 nm and it is clearly observed that the incorporated Bi_2S_3 nanorods can slightly increase the optical absorption in the hybrid film. Moreover, there exists a significant absorbance difference from nearly 480 nm to 620 nm, which reveals that the absorption behaviour of the P3HT phase varies after incorporation of the Bi_2S_3 nanorods. It is well known that the characteristics of the P3HT absorption spectrum can be attributed to the interchain interactions, interlayer interactions or the crystallinity of P3HT.[44–47] Namely, the shoulders at 560 nm and 610 nm are related to the crystalline stacking of the P3HT lamella structure.[44–47] Since we used a 1 : 1 wt/wt ratio of P3HT and the Bi_2S_3 nanorods in the $P3HT/Bi_2S_3$ solution preparation, it can be speculated that, considering the density of P3HT (~1.1 g cm^{-3}) and Bi_2S_3 (~6.8 g cm^{-3}), the P3HT and Bi_2S_3 nanorods occupy 86 vol% and 14 vol% in the $P3HT/Bi_2S_3$ hybrid film, respectively. Additionally, the film thickness of the pristine P3HT film and the $P3HT/Bi_2S_3$ hybrid film are around 100 nm and 130 nm, respectively, obtained by α-stepper.
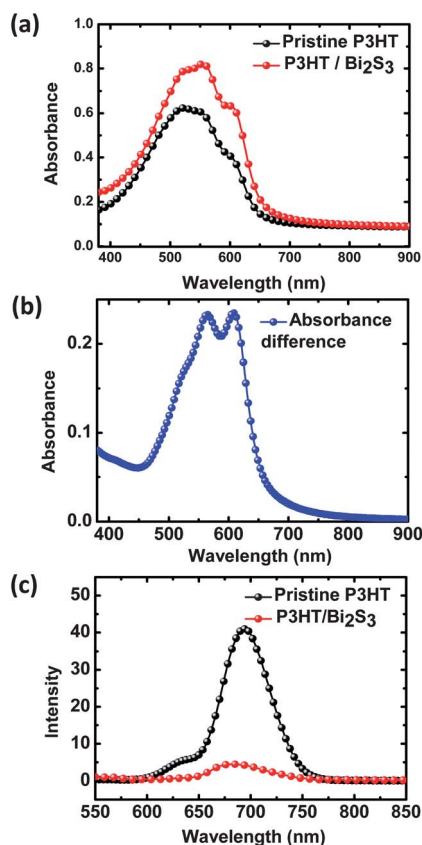
Fig. 6 Comparison of the optical properties between P3HT and the P3HT : Bi$_2$S$_3$ hybrid, (a) absorption spectra, (b) absorbance difference obtained from subtracting the absorption spectrum of pristine P3HT and the P3HT : Bi$_2$S$_3$ hybrid and (c) the photoluminescence spectra.

Therefore, although part of the space is replaced by the Bi$_2$S$_3$ nanorods after their incorporation into the P3HT matrix, there is still 12% more P3HT by volume through which the incidence light passes as compared with the pristine P3HT film. Consequently, this directly results in a positive absorption difference within the region of P3HT absorption (from 480 nm to 650 nm) as shown in Fig. 6(b). Moreover, looking at the more significantly positive absorption difference at 560 nm, which results from the more ordered P3HT, the absorbance is enhanced from 0.58 to 0.82. Considering the definition of absorbance (optical density), A:

$$A = \log_{10}\left(\frac{I_0}{I}\right)$$

where I is the transmitted light intensity and I_0 is the incident light intensity, we found that the light harvesting efficiency, $(1 - I/I_0) \times 100\%$, is enhanced by 15% (from 74% to 85%), which is larger than the value of 12% due to the film thickness effect. These results indicate that there are more efficient π–π* transitions and, thus, an improved crystallinity and enhanced inter-layer and intralayer interactions of P3HT are achieved after incorporation of the Bi$_2$S$_3$ nanorods. Fig. 6(c) shows the PL spectra of pristine P3HT and the P3HT : Bi$_2$S$_3$ hybrid. The pristine P3HT was also prepared under identical fabrication parameters. Similarly, the signal in the PL spectra is contributed

to completely by P3HT and the photoluminescence of inorganic nanorods was not detectable. Considerable quenching in the PL spectra was clearly observed, which can be attributed to the type II energy alignment between P3HT and the Bi$_2$S$_3$ nanorods. Competitive processes, such as exciton dissociation or other forms of energy transfer, may exist after the addition of Bi$_2$S$_3$ nanorods. Hence, the exciton recombination process is hindered leading to a reduced intensity of the PL spectra by 90%.

Fig. 7a and 7b illustrate the operation principle of the KPFM measurement in the dark and under illumination, respectively. Topographical images (7c, 7d) and surface potential mappings in the dark (7e) and under illumination (7f) are also presented. The topographical images show the film morphology to be smooth with a low root mean square roughness of 7.1 nm, indicating a homogeneous film was obtained. However, from the potential images, there exist some dark dots distributed in the thin film, indicating low surface potential regions. We regard the dark dot regions as Bi$_2$S$_3$-rich regions due to their electron-accepting and hole-donating role in the hybrid film. Upon illumination of the thin film, the average surface potential decreases from 283 mV to 249 mV, leading to a considerable negative shift of 34 mV. Recalling a previous study by our group,[48] the average surface potential of pristine P3HT thin films is almost the same after illumination (difference < 2 mV). Therefore, we attributed the significantly negative shift of P3HT : Bi$_2$S$_3$ after illumination to
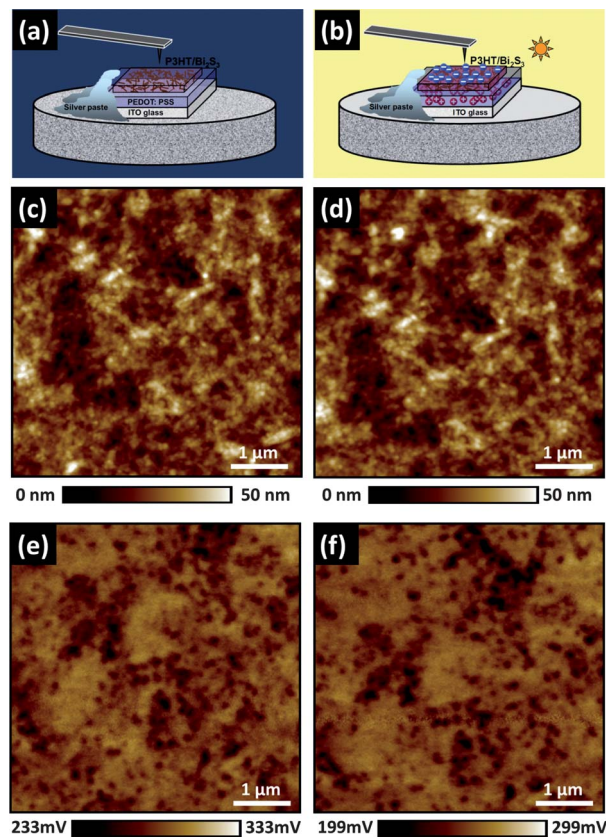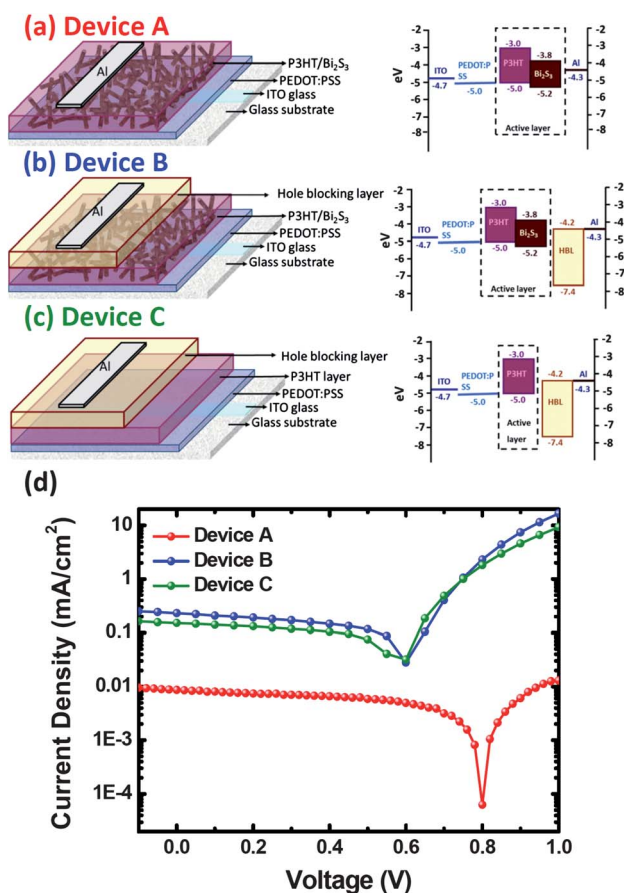

Fig. 7 (a, b) Schematics of the KPFM measurement, (c, d) topographic images of the P3HT : Bi$_2$S$_3$ thin film, (e, f) surface potential images of the P3HT : Bi$_2$S$_3$ thin film. Fig. 7 a, c and e were obtained in dark whereas b, d and f were taken under illumination.

the incorporation of the Bi_2S_3 nanorods. Once the hybrid thin film was excited, the exciton dissociated and the holes grounded to the metal substrate and electrons accumulated on the top of the hybrid layer, indicating the occurrence of a charge separation process between the P3HT and Bi_2S_3 nanorods. We fabricated the devices in a layer-by-layer solution process. First, a structure of device A, ITO/PEDOT : PSS/P3HT : Bi_2S_3/Al, was designed as shown in Fig. 8(a). The band alignment is also presented. This type of structure is typical and the one commonly used in polymer solar cells. From the J–V curve under simulated AM 1.5 illumination (100 mW cm^{-2}) as plotted in Fig. 8(d), the photovoltaic characteristics and open circuit voltage (V_{oc}) of 0.8 volts, which is relatively high for polymer solar cells (typically from 0.5–0.7 V), can be found. The high V_{oc} can be attributed to the large energy gap between the CB of the Bi_2S_3 nanorods (-3.8 eV) and the HOMO of P3HT (-5.0 eV). However, we also found that the current density of device A is extremely low (0.008 mA cm^{-2}). based on a polymer/low band gap nanocrystal hybrid, has recently been reported in the literature and it was found that it usually exhibits a low current density compared to polymer/conventional nanocrystals hybrids (TiO$_2$, ZnO, CdSe, *etc*). Ginger *et al.* employed photoinduced absorption (PIA) spectroscopy to analyze the P3HT/PbSe hybrid.[49] Even though PL quenching was observed from the P3HT/PbSe hybrid, there was no evidence of a long-lived carrier between P3HT and the PbSe

nanocrystal from the PIA analysis, which indicates an inefficient carrier dissociation. In the present study, we have obtained a similar result from the PL measurements with a significant quenching of the P3HT : Bi_2S_3 hybrid. However, in contrast to the PIA results demonstrated by Ginger *et al.* for the P3HT/PbSe hybrid, our KPFM measurements provide evidence of carrier dissociation and negative carrier accumulation of the P3HT : Bi_2S_3 hybrid under illumination. Therefore, we attribute the low current density to the inefficient electron extraction from the top of the film, resulting from either crystal defects or the trap states of Bi_2S_3. In order to effectively collect electrons at the electrode, we incorporated an electron transport layer (hole blocking layer (HBL)) comprised of TiO$_2$ nanorods sandwiched between the active layer and the Al electrode. The structure of device B is illustrated in Fig. 8(b). From the J–V curve plotted in Fig. 8(d), we observed that the current density is improved by a factor of 28 (from 0.008 mA cm^{-2} to 0.230 mA cm^{-2}); however, a lower V_{oc} of 0.60 V is obtained. The lower V_{oc} is expected from the band alignment also shown in Fig. 8(b). The inclusion of the TiO$_2$ layer constructs a cascade-type energy alignment among P3HT : Bi_2S_3/TiO$_2$, leading to a theoretically decreased V_{oc} of the energy gap between the CB of TiO$_2$ (-4.2 eV) and the HOMO of P3HT (-5.0 eV). Although this sacrifices the value of V_{oc}, the TiO$_2$ layer indeed benefits the electron collection resulting in a considerable improvement in the current density. It is noteworthy that the P3HT/TiO$_2$ interface also constructs a type II alignment between the two layers. Therefore, for the sake of comparison, we fabricated a third device, C, from a pristine P3HT/TiO$_2$ bi-layer structure, as shown in Fig. 8(c). The J–V curve of the device plotted in Fig. 8 (d) shows a current density of 0.15mA cm^{-2}. Dividing the J_{sc} values of curve B and curve C (0.08 mA cm^{-2}), it is interesting to note that the P3HT : Bi_2S_3 bulk heterojunction truly contributes to the current density but can not be drawn out in the absence of a TiO$_2$ layer (0.008 mA cm^{-2} of device A).

4. Conclusions

Bi_2S_3 nanorods were synthesized successfully and the synthesis conditions were systematically investigated. Bi_2S_3 nanorods grown at 130 °C for 30 min yielded nanorods with good crystallinity and suitable dimensions for applications in P3HT : Bi_2S_3 hybrid solar cells. The as synthesized nanorods exhibit a band gap of 1.4 eV and construct a type II band alignment with P3HT. The results of an optical properties investigation suggest the inclusion of Bi_2S_3 nanorods in the hybrid film affects light harvesting slightly, helps the stacking of a P3HT ordered structure and hinders the charge recombination of P3HT. Surface potential mapping of the P3HT : Bi_2S_3 film, measured by KPFM, provides information on the electron accumulation at the top of the film and charge transfer between the polymer-rich domains and the nanocrystal-rich domains under illumination. Photovoltaic characteristics were observed from devices based on the P3HT : Bi_2S_3 hybrid and the current density contributed to by the heterojunction was also obtained. This study, which focused on P3HT : Bi_2S_3 hybrids, showcases a new candidate for the fabrication of low-cost and environmentally friendly polymer : inorganic hybrid solar cells.

Fig. 8 (a, b, c) Illustrations of the three different device structures and (d) J–V curves of device A (red), B (blue) and C (green).

Acknowledgements

Notes and references

1 M. J. Fernée, B. N. Littleton, S. Cooper, H. Rubinsztein-Dunlop, D. E. Gómez and P. Mulvaney, *J. Phys. Chem. C*, 2008, **112**, 1878.
2 B. Comiskey, J. D. Albert, H. Yoshizawa and J. Jacobson, *Nature*, 1998, **394**, 253.
3 F. Miomandre, P. Audebert, J. P. Bonnet, A. Brosseau, P. Perriat, C. Weisbuch, W. Wen and P. Sheng, *J. Nanosci. Nanotechnol.*, 2008, **8**, 4353.
4 R. M. Stevenson, R. J. Young, P. Atkinson, K. Cooper, D. A. Ritchie and A. J. Shields, *Nature*, 2006, **439**, 179.
5 S. Santra, H. Yang, D. Dutta, J. T. Stanley, P. H. Holloway, W. Tan, B. M. Moudgil and R. A. Mericle, *Chem. Commun.*, 2004, 2810.
6 X. Gao, Y. Cui, R. M. Levenson, L. W. K. Chung and S. Nie, *Nat. Biotechnol.*, 2004, **22**, 969.
7 T. Paunesku, T. Rajh, G. Wiederrecht, J. Maser, S. Vogt, N. Jićević, M. Protić, B. Lai, J. Oryhon, M. Thurnauer and G. Woloschak, *Nat. Mater.*, 2003, **2**, 343.
8 E. Lifshitz, M. Brumer, A. Kigel, A. Sashchiuk, M. Bashouti, M. Sirota, E. Galun, Z. Burshtein, A. Q. Le Quang, I. Ledoux-Rak and J. Zyss, *J. Phys. Chem. B*, 2006, **110**, 25356.
9 A. L. Rogach, N. Gaponik, J. M. Lupton, C. Bertoni, D. E. Gallardo, S. Dunn, N. L. Pira, M. Paderi, P. Repetto, S. G. Romanov, C. O'Dwyer, C. M. S. Torres and A. Eychmiiler, *Angew. Chem., Int. Ed.*, 2008, **47**, 6538.
10 N. P. Gaponik, D. V. Talapin and A. L. Rogach, *Phys. Chem. Chem. Phys.*, 1999, **1**, 1787.
11 P. V. Kamat, *J. Phys. Chem. C*, 2008, **112**, 18737.
12 M. G. Panthani, V. Akhavan, B. Goodfellow, J. P. Schmidtke, L. Dunn, A. Dodabalapur, P. F. Barbara and B. A. Korgel, *J. Am. Chem. Soc.*, 2008, **130**, 16770.
13 I. Robel, V. Subramanian, M. Kuno and P. V. Kamat, *J. Am. Chem. Soc.*, 2006, **128**, 2385.
14 M. Afzaal and P. O'Brien, *J. Mater. Chem.*, 2006, **16**, 1597.
15 K. S. Leschkies, R. Divakar, J. Basu, E. Enche-Pommer, J. E. Boercker, C. B. Carter, U. R. Kortshagen, D. J. Norris and E. S. Aydil, *Nano Lett.*, 2007, **7**, 1793.
16 Z. A. Peng and X. Peng, *J. Am. Chem. Soc.*, 2002, **124**, 3343.
17 B. Sun and N. C. Greenham, *Phys. Chem. Chem. Phys.*, 2006, **8**, 3557.
18 K. T. Yong, Y. Sahoo, M. T. Swihart and P. N. Prasad, *J. Phys. Chem. C*, 2007, **111**, 2247.
19 G. Li, V. Shrotriya, J. Huang, Y. Yao, T. Moriarty, K. Emery and Y. Yang, *Nat. Mater.*, 2005, **4**, 864.
20 W. Ma, C. Yang, X. Gong, K. Lee and A. J. Heeger, *Adv. Funct. Mater.*, 2005, **15**, 1617.
21 H. Y. Chen, J. Hou, S. Zhang, Y. Liang, G. Yang, Y. Yang, L. Yu, Y. Wu and G. Li, *Nat. Photonics*, 2009, **3**, 649.
22 T. W. Zeng, Y. Y. Lin, H. H. Lo, C. W. Chen, C. W. Chen, S. C. Liou, H. Y. Huang and W. F. Su, *Nanotechnology*, 2006, **17**, 5387.
23 W. U. Huynh, J. J. Dittmer and A. P. Alivisatos, *Science*, 2002, **295**, 2425.
24 W. J. E. Beek, M. M. Wienk and R. A. J. Janssen, *Adv. Mater.*, 2004, **16**, 1009.
25 Y. Y. Lin, T. H. Chu, S. S. Li, C. H. Chuang, C. H. Chang, W. F. Su, C. P. Chang, M. W. Chu and C. W. Chen, *J. Am. Chem. Soc.*, 2009, **131**, 3644.
26 B. Sun and N. C. Greenham, *Phys. Chem. Chem. Phys.*, 2006, **8**, 3557.
27 B. Sun, H. J. Snaith, A. S. Dhoot, S. Westenhoff and N. C. Greenham, *J. Appl. Phys.*, 2005, **97**, 014914.
28 N. C. Greenham, X. Peng and A. P. Alivisatos, *Phys. Rev. B: Condens. Matter*, 1996, **54**, 17628.
29 W. J. E. Beek, M. M. Wienk and R. A. J. Janssen, *J. Mater. Chem.*, 2005, **15**, 2985.
30 D. M. Guldi, I. Ziberman, G. Anderson, N. A. Kotov, N. Tagmatarchis and M. Prato, *J. Mater. Chem.*, 2005, **15**, 114.
31 H. M. P. Wong, P. Wang, A. Abrusci, M. Svensson, M. R. Andersson and N. C. Greenham, *J. Phys. Chem. C*, 2007, **111**, 5244.
32 S. Dayal, N. Kopidakis, D. C. Olson, D. S. Ginley and G. Rumbles, *Nano Lett.*, 2010, **10**, 239.
33 S. A. Mcdonald, G. Konstantatos, S. Zhang, P. W. Cyr, E. F. D. Klem, L. Levina and E. H. Sargent, *Nat. Mater.*, 2005, **4**, 138.
34 D. Cui, J. Xu, T. Zhu, G. Paradee and S. Ashok, *Appl. Phys. Lett.*, 2006, **88**, 183111.
35 E. Arici, H. Hoppe, F. Schäffler, D. Meissner, M. A. Malik and N. S. Saricifci, *Thin Solid Films*, 2004, **451–452**, 612.
36 Y. Y. Lin, D. Y. Wang, H. C. Yen, H. L. Chen, C. C. Chen, C. M. Chen, C. Y. Tang and C. W. Chen, *Nanotechnology*, 2009, **20**, 405207.
37 G. Konstantatos, L. Levina, J. Tang and E. H. Sargent, *Nano Lett.*, 2008, **8**, 4002.
38 A. A. Tahir, M. A. Ehsan, M. Mazhar, K. G. U. Wijayantha, M. Zeller and A. D. Hunter, *Chem. Mater.*, 2010, **22**, 5084.
39 R. Malakooti, L. Cademartiri, Y. Akçakir, S. Petrov, A. Migliori and G. A. Ozin, *Adv. Mater.*, 2006, **18**, 2189.
40 M. C. Wu, H. C. Liao, Y. Chou, C. P. Hsu, W. C. Yen, C. M. Chuang, Y. Y. Lin, C. W. Chen, Y. F. Chen and W. F. Su, *J. Phys. Chem. B*, 2010, **114**, 10277.
41 M. B. Sigman and B. A. Korgel, *Chem. Mater.*, 2005, **17**, 1655.
42 E. Z. da Silva, A. J. R. da Silva and A. Fazzio, *Phys. Rev. Lett.*, 2001, **87**, 256102.
43 D. Wang, J. Zhao, S. Hu, X. Yin, S. Liang, Y. Liu and S. Deng, *Nano Lett.*, 2007, **7**, 1208.
44 S. Jeong, Y. Kwon, B. D. Choi, G. Kwak and Y. S. Han, *Macromol. Chem. Phys.*, 2010, **211**, 2474.
45 Y. Kim, S. Cook, S. M. Tukadhar, S. A. Choulis, J. Nelson, J. R. Durrant, D. D. C. Bradley, M. Giles, I. Mcculloch, C. Ha and M. Ree, *Nat. Mater.*, 2006, **5**, 197.
46 P. J. Brown, D. S. Thomas, A. Köhler, J. S. Wilson and J. S. Kim, *Phys. Rev. B: Condens. Matter*, 2003, **67**, 064203.
47 B. Peng, X. Guo, Y. Zou, C. Pan and Y. Li, *J. Phys. D: Appl. Phys.*, 2011, **44**, 365101.
48 M. C. Wu, Y. J. Wu, W. C. Yen, H. H. Lo, C. F. Lin and W. F. Su, *Nanoscale*, 2010, **2**, 1448.
49 K. M. Noone, N. C. Anderson, N. E. Horwitz, A. M. Munro, R. P. Kulkarni and D. S. Ginger, *ACS Nano*, 2009, **3**, 1345.